Wind tunnel analysis of the slipstream and wake of a high-speed train

J.R. Bell [a,*], D. Burton [a], M. Thompson [a], A. Herbst [b], J. Sheridan [a]

[a] Department of Mechanical and Aerospace Engineering, Monash University, Clayton, Victoria 3800, Australia
[b] Centre of Competence for Aero- and Thermodynamics, Bombardier Transportation, Vasteras, Sweden

ARTICLE INFO

ABSTRACT

The slipstream of high-speed trains is investigated in a wind tunnel through velocity flow mapping in the wake and streamwise measurements with dynamic pressure probes. The flow mapping is used to explain the familiar slipstream characteristics of high-speed trains, specifically the largest slipstream velocities in the near wake. Further, the transient nature of the wake is explored through frequency and probability distribution analysis. The development of a wind tunnel methodology for slipstream assessment is presented and applied, comparing the output to full-scale results available in the literature. The influence of the modelling ballast and rail or a flat ground configuration on the wake structure and corresponding slipstream results are also presented.

© 2014 Elsevier Ltd. All rights reserved.

1. Introduction

The slipstream of a high-speed train (HST) continues to be an important aspect of aerodynamic performance and safe operation. Slipstream is the air flow induced by the train's movement as experienced by a stationary observer. Such flows can be hazardous to waiting commuters at platforms and track-side workers (Pope, 2007). The flows can also cause damage to track-side infrastructure. Regulations are currently in place aimed at reducing risks for HSTs; for example, the European Railway Agency's (2008) (ERA) Technical Specifications for Interoperability (TSI) and the European industry norms outlined by the European Committee for Standardization (EN) (CEN European Standard, 2009). Thus, there is a need for both improvement in the understanding of the slipstream of HSTs and methodologies for testing HSTs in the development stages.

The slipstream of a HST under 'standard operation and configuration', defined here as a single train with one nose and one tail travelling on a straight track over flat ground with no crosswind present, is investigated. This idealised train is modelled to isolate the slipstream characteristics generated by the train's essential generic geometry in an ideal environment. Under these conditions, the slipstream of a HST has a local peak velocity at the nose passing, a gradual increase in velocity as the boundary layer develops along the length of the train, followed by the largest peak in the near wake of the vehicle (Baker, 2010; Baker et al., 2001, 2012a,b). These slipstream characteristics correspond to the description by Baker (2010) of flow around a HST having three distinct regions: nose, boundary layer and wake regions. These general characteristics of a HST's slipstream, illustrated in Fig. 1, are referred to herein as the 'standard slipstream profile' and have been found by a number of researchers in full-scale track-side experiments (Baker, 2010; Baker et al., 2012a,b; Sterling et al., 2008).

Inter-carriage gaps have been found to cause perturbations to this general description as peaks, troughs or waves (Muld et al., 2013b; Pii et al., 2014; Bell et al., 2014), however these do not appear to significantly change the rate of increase of the boundary layer thickness. A local tail peak has also been identified in a number of HST slipstream profiles in full-scale experiments (Baker et al., 2012a), scaled experiments (Gilbert et al., 2013), and numerical simulations (Muld et al., 2013b; Hemida et al., 2013), but is not a standard feature and is likely dependent on geometry and measurement position. Both features are included in Fig. 1 as dotted lines to indicate that they are not standard, nor the focus of this research. Further, as the flow around HSTs is highly three dimensional, the slipstream profile as measured by a single streamwise line, as indicated in Fig. 1, is highly sensitive to measurement position, with the shape of the slipstream profile – even the relative magnitudes of the peaks – being susceptible to changes. However, in general the slipstream velocity decreases with increasing height above ground and distance away from train, as shown in full-scale experiments (Sterling et al., 2008) and numerical simulations (Hemida et al., 2013).

A number of known flow mechanisms can be identified in the wake of a high-speed train: shear layers, von Kármán-type vortex shedding, separation and recirculation regions and a pair of twin counter-rotating longitudinal vortices (Morel, 1980; Weise et al.,
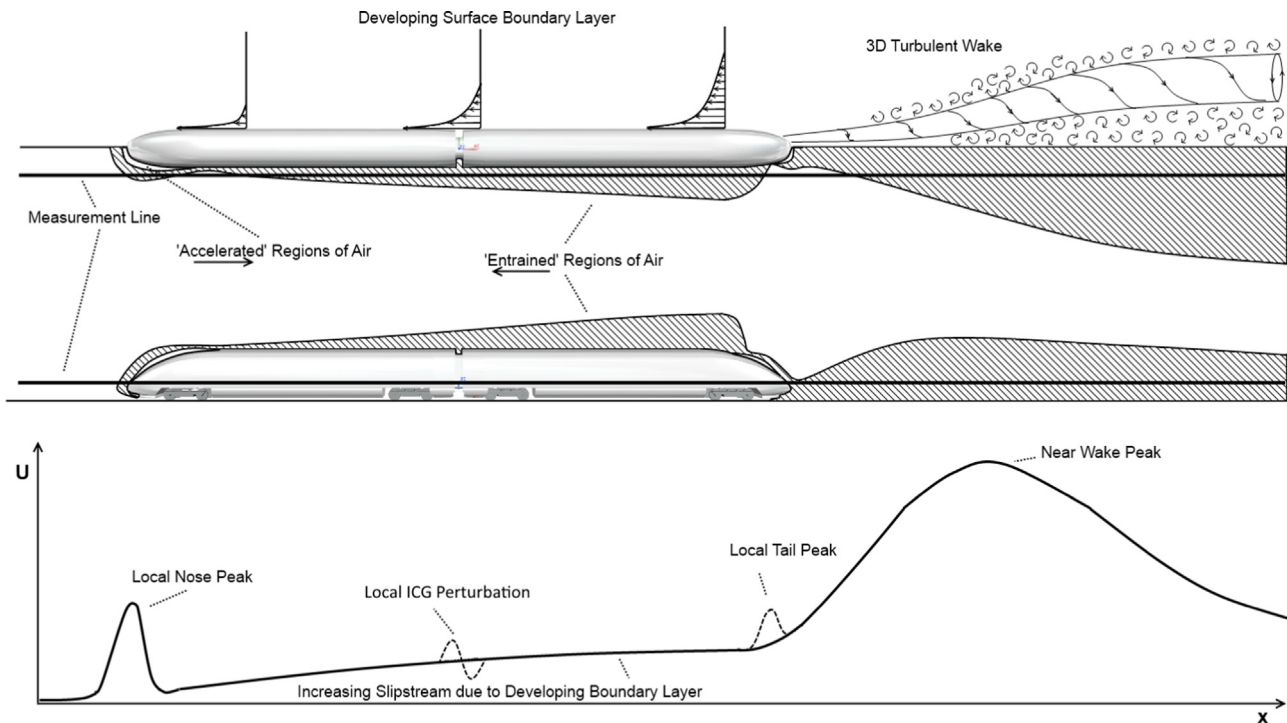

Fig. 1. The slipstream of a high-speed train. The flow induced can travel in two directions: 'Accelerated' flow – travelling opposite to the direction the train is travelling and 'Entrained' flow – travelling in the direction the train is travelling. Accelerated flow is primarily around the head and tail. Increasing thickness of the entrained flow exists over the roof and sides due to the thickening boundary layer. Similarly, a widening region of entrained flow occurs in the wake, expected to be due to the presence of coherent turbulent structures of different scales within the wake. The perturbation in the developing boundary layer – due to the inter-carriage gap – and the local peak at the tail are presented as dotted lines to indicate that they are not found in all HST slipstream profiles.

2006; Muld et al., 2012). The contribution of twin counter-rotating vortices to wake topology has been identified as a particularly important feature in characterising slipstream (Baker, 2010; Weise et al., 2006; Muld et al., 2012). These vortices move downwards and outwards due to the mutual induction and interaction with the ground as they progress away from the vehicle (Weise et al., 2006; Muld et al., 2012; Heine et al., 2013; Schulte-Werning et al., 2001; Yao et al., 2013), with some researchers predicting that they exhibit spanwise oscillations (Muld et al., 2012; Yao et al., 2013; Schulte-Werning et al., 2003).

The counter-rotating vortices are created by the interaction between the down-wash over the roof and tail of the train and the flow around the sides of the train in the transition from a constant cross-section to the end of the tail. Other bluff body ground vehicles such as cars also contain a pair of counter-rotating vortices in the wake, and have been researched extensively primarily motivated by drag reduction. Such research, such as the widely referenced `Ahmed body' (Ahmed, 1983), is not necessarily due to the uniqueness of HST geometry; slender (high length:height), small aspect ratio (height:width ratio ≈ 1) and streamlined nose/tail with no fixed separation points.

The link between a HST's wake topology and its slipstream has not been explicitly established in the literature. Further, full-scale experiments (Baker et al., 2012a,b; Sterling et al., 2008), scaled experiments (Baker, 2010; Bell et al., 2014) and numerical investigations (Muld et al., 2013b; Pii et al., 2014; Hemida et al., 2013) have found high run-to-run variance, which suggests that understanding the transient wake in addition to the time averaged wake is necessary to understand slipstream. The work presented aims to bridge this gap.

Insight into the time-averaged wake and its transient features is achieved by utilising the train-fixed frame-of-reference in a wind tunnel methodology to perform time-averaged flow mapping and point-wise frequency and probability distribution analysis. This is the primary benefit of the wind tunnel methodology, the ability to map the flow. A wind tunnel methodology does however have a number of limitations. The train-fixed frame-of-reference does not easily allow for gust analysis, currently used to measure a HST's slipstream performance in the typical sense, as individual runs are not captured. Further, the presence of a stationary floor in wind tunnels rather than using a rolling road or suction results in a boundary layer developing on the floor, which does not occur in full-scale operation.

The presence of a stationary floor is a common experimental limitation for many wind tunnel experiments and one that is only mitigated with difficult and costly solutions such as boundary layer suction or a moving floor (rolling road). Experiments by Kwon et al. (2001) highlight the difficulty of such solutions to HST investigations due to their long bodies, having to apply suction at multiple slot locations with great care, noting that their position could influence drag measurements. Further, inclusion of a track and ballast shoulder ground configuration, as discussed below, prevents such boundary layer treatments.

The effect of a stationary floor on the aerodynamics of ground vehicles has been investigated by a number of researchers, with primary concern on the influence on drag and lift prediction (Choi et al., 2014). No definitive effect has been established, with the magnitude and even direction of the effect on lift and drag varying with geometry and distance to the ground (Choi et al., 2014). Vehicles with rear diffuser-type geometry have been found to be most susceptible to the influence of floor motion (Bearman et al., 1988). Some researchers have investigated the influence floor motion has on the near-wake structure. Scaled experiments by Bearman et al. (1988) and Strachan et al. (1988), and numerical simulations by Krajnović and Davidson (2005) have found that the pair of counter-rotating longitudinal vortices, which develop over

the C-pillar of generic automotive vehicles – structures similar to that dominating the wake of the HST presented in this work – were largely insensitive to the stationary floor in the near wake.

Large Eddy Simulations (LES) of Krajnović and Davidson (2005) at a Reynolds number of 2×10^5 indicated that the stationary floor influenced the base pressure, and reduced the clarity of dominant frequencies found in the transient flow. Despite this, velocity profiles at multiple distances in the near wake displayed only minor differences between a moving and stationary floor in close proximity to the ground, leading the authors to conclude that the longitudinal vortices were relatively insensitive to ground effect. The scaled experiments by Bearman et al. (1988) presented velocity profiles from pulsed-wire anemometry together with drag and lift measurements which indicate that the effect of a moving floor was negligible for a Davis generic automotive model with zero upsweep angle. Similarly, Strachan et al. (1988) noted that the C-pillar vortices of an Ahmed body were insensitive to the motion of the floor in their scaled experiments at a Reynolds number of 1.7×10^6 (based on length) with a rolling road based on velocity profiles obtained from Laser Doppler Anemometry (LDA). Kwon et al. (2001) in scaled wind-tunnel experiments identified differences in oil-flow visualisation on the floor with and without tangential blowing, with a more coherent pattern and greater spanwise dispersion of the wake with tangential blowing. However, of course, it is expected that any differences in the wake would be greatest on the floor surface, and although outright drag coefficients exhibited minor differences for the same model between moving floor, tangential blowing and stationary cases, the change in drag coefficient was consistent across all floor treatments for a number of changes to geometry.

Scaled model experiments to assess slipstream have been performed at moving model facilities (Baker, 2010; Bell et al., 2014; Gilbert et al., 2013). The moving model results in the correct relative motion between the ground and the model, thus no ground boundary layer develops as in stationary floor wind tunnel experiments. This methodology also has the benefit of the ground-fixed frame-of-reference as in full-scale experiments, allowing gust analysis of individual runs to be performed. A moving model experiment also has limitations, where approximately 20 (CEN European Standard, 2009) runs are required to obtain statistically stable measurements in transient areas, such as the near wake of a HST. Flow mapping in the near wake, within the path of the vehicle is also very difficult and has only recently been proved possible using high speed Particle Image Velocimetry (PIV) by Heine et al. (2013).

Two ground configurations: 'true flat ground' (FG) and 'single track ballast and rail' (STBR) are common in experimental and numerical investigations. Ground configuration is not specified in the EN for scaled model slipstream experiments, however STBR was required for head pressure pulse investigations in the 2009 EN (CEN European Standard, 2009) – the 2013 EN (CEN European Standard, 2013) revision excluded the rails from this configuration – and crosswind investigations (CEN European Standard, 2010). The STBR ground configuration has also been proposed to be better suited to stationary floor experiments as it potentially lifts the model out of the ground boundary layer (Schober et al., 2010). The latter proposed benefit of using STBR assumes that the boundary layer does not develop over the STBR to the same extent as for a flat floor. The sensitivity of slipstream results to a STBR or FG configuration was investigated and is presented in this work.

The reduced length-to-height ratio (L/H) is necessary to allow as large a scale model in a test section – in order to achieve high Reynolds numbers. This is also a limitation of moving model experiments for similar practical reasons. The high L/H of HSTs also presents a challenge numerically as although technically they are not limited in space, computational resources become an issue,

with increased L/H coming at the cost of Reynolds number and grid refinement. Although acknowledged in the literature (Weise et al., 2006), L/H has only recently been investigated by Muld et al. (2013a), and the effect of L/H has yet to be explicitly quantified.

This work, part of a collaboration between Monash University and Bombardier Transportation, aims to investigate wind tunnel testing and analysis techniques for use as a methodology for assessing the slipstream of HSTs. If an analysis technique can be developed for translating the data and predictions from wind tunnel measurements to standard train reference frame the authors believe that wind tunnel testing will offer significant benefits complementing other methodologies, particularly during the prototype phase of HST development. The experimental investigation presented includes streamwise measurements with dynamic pressure probes, to which the first iteration of a method for performing gust analysis in the manner specified by the TSI regulations, in the train-fixed frame-of-reference, has been applied. The presented flow mapping in the wake, also with dynamic pressure probes, aids in the identification and quantification of the flow mechanisms responsible for the transient characteristics which affect TSI-type analysis and thereby improve the understanding and predictive capabilities of the slipstream and wake structure of high-speed trains.

2. Methodology

2.1. Experimental setup

A 1/10 scale Aerodynamic Train Model (ATM) – a simplified version of the Inter-City-Express 2 (ICE2) high-speed train in operation throughout Germany – was used in the experimental work. The experiment was performed in the Monash University 450 kW wind tunnel. The wind tunnel is a closed circuit design, with a variable pitch axial fan driven by a 450 kW motor capable of producing wind speeds between 5 and 40 m/s.

Fig. 2 shows the experimental setup in the wind tunnel and the coordinate system adopted. X values are normalised by the model height, $x=0$ corresponding to the tail, as is the practice in general ground vehicle aerodynamics (Bearman et al., 1988; Krajnović and Davidson, 2005). In addition, the authors believe that the near wake is to be dominated by the tail geometry. Y values are normalized by the half of the model width, looking windward, $y=-1$ corresponds to the left vertical edge, $y=1$ to the right edge. Z values are normalised by the model height, with $z=0$ corresponding to the top of rail (TOR). Thus the z values presented are above top of rail (ATOR).

The closed test section measures $2(4.9H) \times 2$ m and was fitted with a 0.5 m ($1.2H$) high splitter plane to reduce ground boundary layer effects, resulting in a cross sectional area above the splitter plane of 3.0 m^2

The ATM measured $3.5(8.5H) \times 0.3 \times 0.41$ m ($L \times W \times H$), with a cross sectional area of 0.123 m^2. The model had three sets of bogies, no pantographs, no inter-carriage gaps, as the essential geometry – the gross external shape – is the focus of this investigation. The model was supported by two 25 mm wide streamlined centred supports, which connected the model to the floor of the wind tunnel.

Two ground configurations that adhere to the EN (CEN European Standard, 2009, 2010) were modelled; the effect of the ballast configuration including rails, adhering to the 2009 EN (CEN European Standard, 2009) and the revised 2013 EN (CEN European Standard, 2013) was not investigated but is not expected to be significant. A 1/10th scale single track ballast and rail (STBR) ground configuration (see Fig. 3a) was utilised with height of 100 mm ($0.24H$) and upper and lower widths of 300 mm ($1W$) and
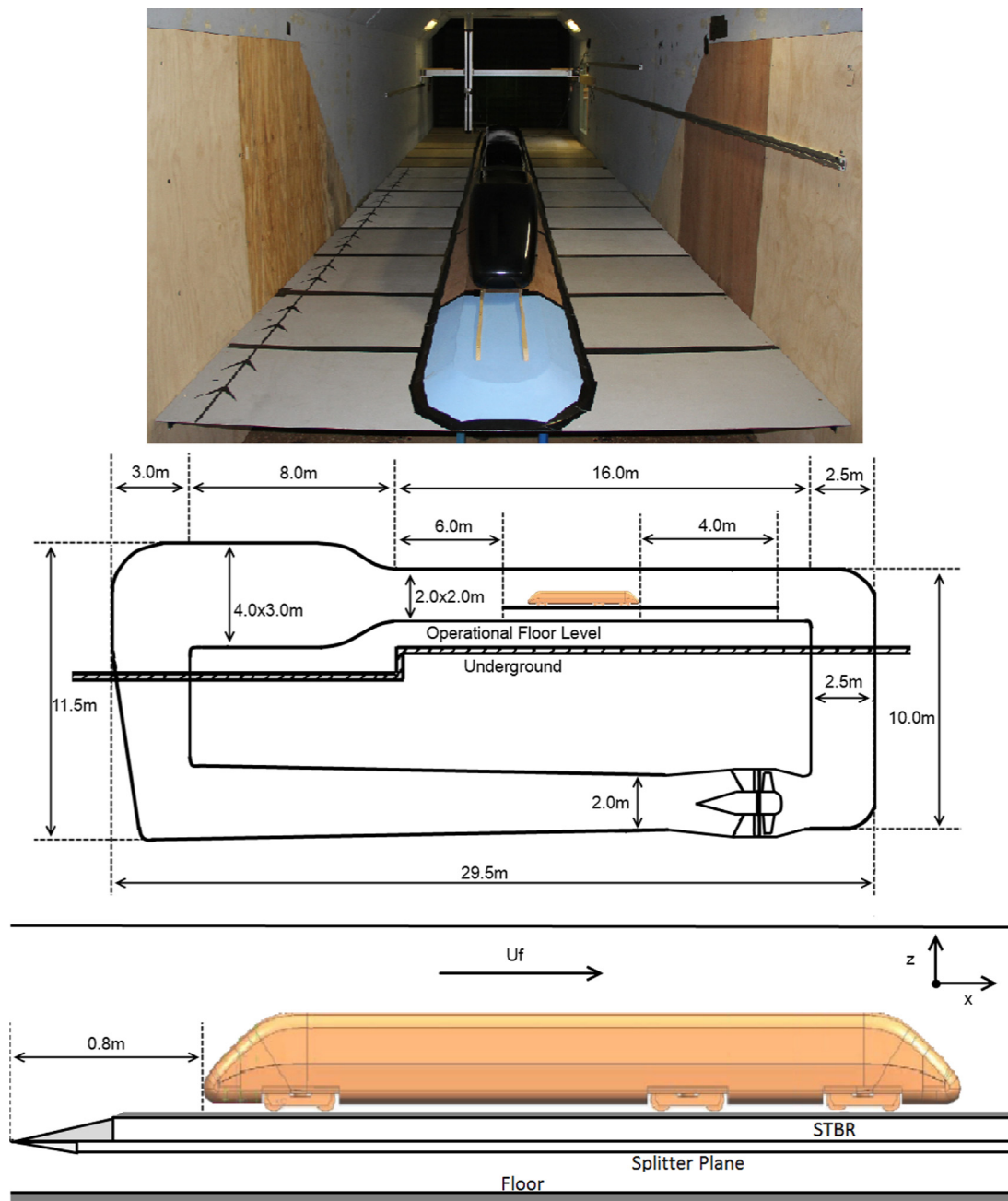
Fig. 2. Experimental setup in the Monash 450 kW wind tunnel with 1:10 scale ICE2 model. A 500 mm high splitter plate was utilised to reduce the ground boundary layer.

555 mm (1.85W) respectively, adhering to the EN (CEN European Standard, 2009). The leading edge of the STBR had a front angle equivalent to the side angle (32°) swept 180°. A true flat ground (FG) configuration (see Fig. 3b) was also modelled, where no ballast or rail was included, and the wheels of the train were 23.5 mm (0.06H) (equivalent to 0.235 m in full-scale) above the ground. Velocity measurements, as per Section 2.2, established that no separation occurred over the leading edge of the STBR. Consequently, the boundary layer thicknesses over and next to the STBR were equivalent to the FG configuration.

The maximum blockage ratio was $\approx 7\%$, including blockage due to the traverse and STBR. The approximate turbulence intensity (I_{uvw}) above the wind tunnel boundary layer was 1%.

The stationary floor and reduced length–height ratio (model $L/H=9$, full-scale $L/H=50$) of the model tested potentially results in differences in the development of a relative boundary layer

height to full-scale. Sensitivity of the results to Reynolds number over the range 4×10^5–7×10^5, with width as the characteristic length (corresponding to freestream velocities of 20–37 m/s), is presented in Section 4.2, however this is still significantly smaller than full-scale Reynolds number of 17×10^6 (corresponding to a full-scale train travelling at 300 km/h). These factors are acknowledged as limitations in the experimental setup, however investigation into the sensitivity of results to these factors are beyond the scope of this paper.

2.2. Measurements

Measurements were taken with a 4-hole dynamic pressure probe (cobra type). Measurements had a sample time of 15 s, enabling statistically stable measurements, and a sampling frequency of 2000 Hz (≈ 460 Hz full-scale), near the upper limit of
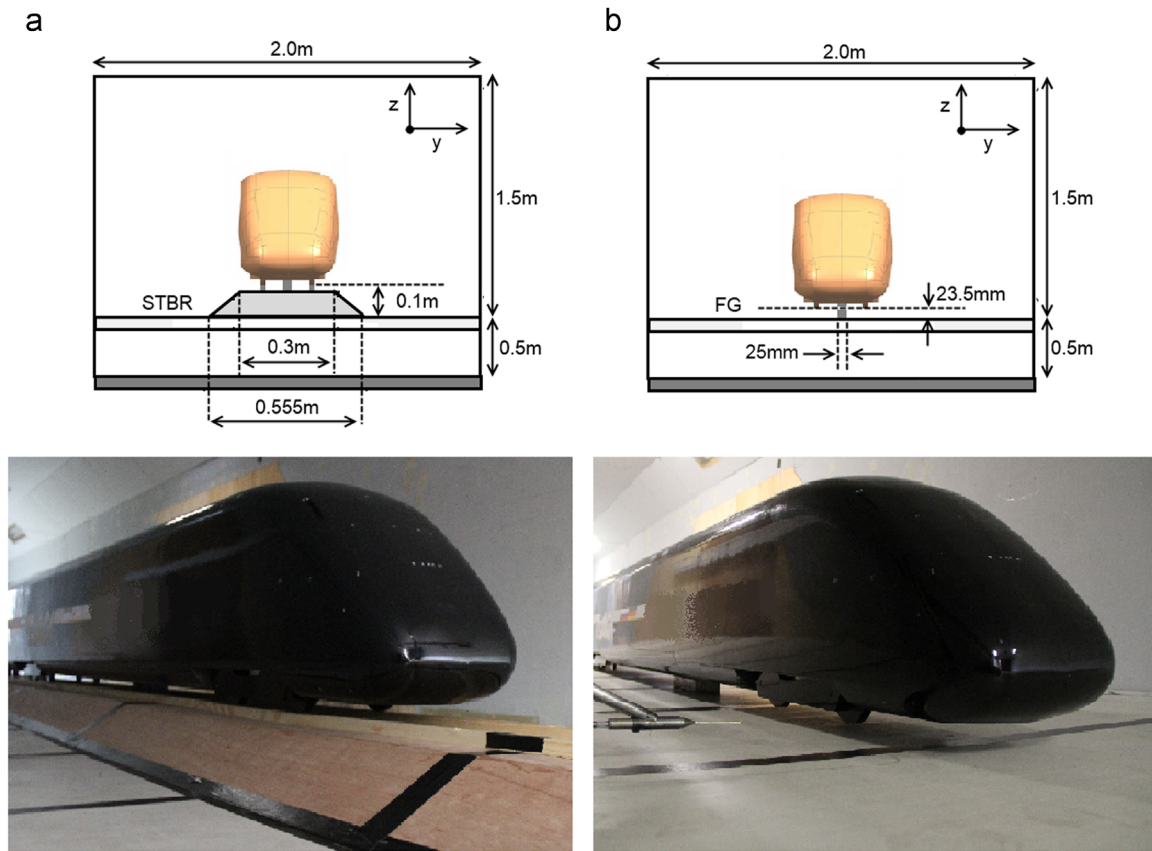
Fig. 3. Ground configurations modelled: the 1:10 scale ICE2 model was mounted on two 25 mm streamlined supports above a 1:10 scale STBR (left) and FG (right). A 500 mm high splitter plate was utilised to reduce the ground boundary layer.

the cobra probe capabilities. The cobra probe is capable of determining velocities with the accuracy of ± 1 m/s within a $\pm 45°$-cone angle; however, it is not capable of identifying reversed flow (Hooper and Musgrove, 1997). An indication of the percentage of flow that is outside its calibrated cone of acceptance is provided by the probes accompanying software, in all cases reported, 95% of measurements or greater were within the cone of acceptance.

The size of the probe is also expected to influence the size of the structures it can resolve. The cobra probe head has a diameter of 4 mm. It is proposed that it can resolve structures with length scales of 10 times this diameter (40 mm) (Hooper and Musgrove, 1997). This corresponds to a 40 mm ($0.01H$) diameter probe in full scale, with resolvable structures of 0.4 m ($0.1H$) at full-scale. At the freestream speeds measured in the experiment of 20–35 m/s, this length-scale corresponds to structures with time-scales of 0.002–0.001, which require a minimum of 500–900 Hz to resolve, thus the 2000 Hz sampling rate is sufficient.

The cobra probe was moved using an automated mechanical traverse. Streamwise (x direction) sweeps at $y=2$ ($W/2$), $z=0.05H$ ATOR and $z=0.35H$ ATOR equivalent to TSI (European Rail Agency, 2008) 'track-side' and 'platform' heights ($z=0.2$ m and $z=1.44$ m) were recorded. The 'platform' height did not model a physical platform, it is a reference height determined from 1.2 m above the minimum platform height in the TSI of 0.24 m, a height commonly measured in other experiments also without a physical platform.

Further, 6 yz spanwise planes were measured with a square grid of $\approx 0.06H$. Measurements were performed in both the positive and negative y domain, however only with high resolution in the negative (see Fig. 4). Positive y measurements were used to confirm symmetry in the flow, as displayed in Fig. 5.

The longitudinal freestream velocity was observed to increase along the length of the body. This can be explained by the increasing contribution of wall effects of the wind tunnel and train surfaces to freestream velocity speed up, a result of the conservation of volume flow in the wind tunnel.

To account for these effects, velocities measured were normalised using the 'local freestream velocity'. The local freestream velocity was a product of the reference freestream velocity (from an upstream pitot-static tube) and a linear correction function. The linear correction function (see Eq. (1)) was empirically fitted to multiple freestream velocities measured 400 mm above and along the length of the model and into the wake. The linear correction factor applied corresponded to an 0.8% increase in velocity over a longitudinal distance of $1H$:

$$u_L = b(x)u_R, \tag{1}$$

where u_L is the local freestream velocity, u_R the reference freestream velocity, and $b(x)$ the linear correction function.

2.3. Ground and roof boundary layers

The measured displacement thickness of the boundary layer was $0.006H$ and $0.018H$ at the models nose and tail positions respectively in an empty tunnel above the splitter plate, in the FG configuration. The boundary layer profiles are visible in Fig. 6, with the location of the scaled model wheels included for both ground configurations.

The reduced L/H of 9 of the scaled model compared to a full-scale operational train of ≈ 50 could lead to a difference in the level of boundary layer development, the separation point at the tail and the shear layer thickness in the wake. The reduced L/H has
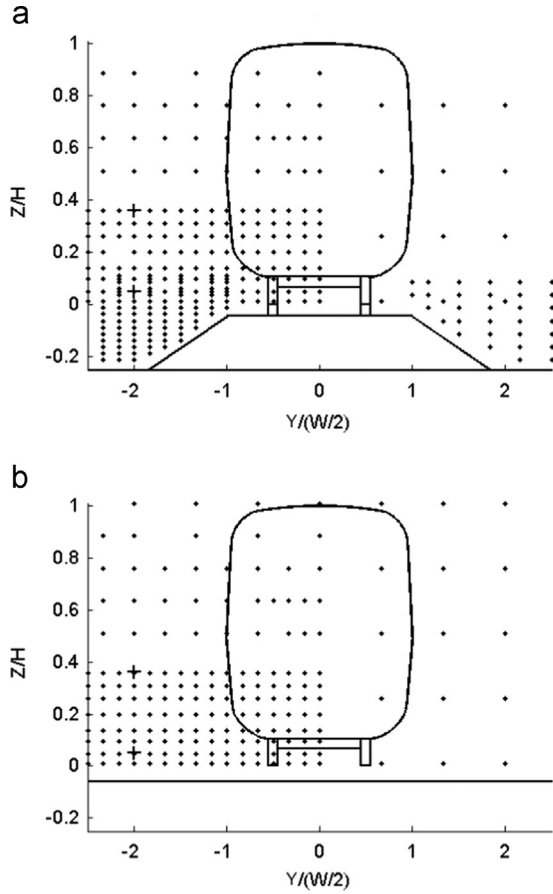
Fig. 4. Cobra probe measurement positions in the *yz* plane for (a) STBR and (b) FG configurations. Higher resolution on LHS and RHS was used to confirm symmetry.
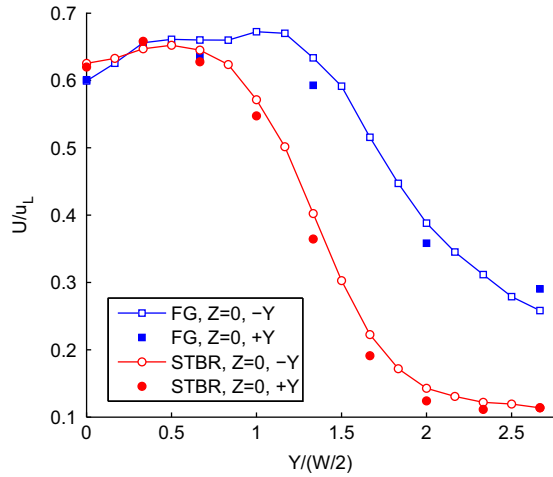

Fig. 5. Cobra probe measurement in the positive and the negative *Y* axis for STBR and FG configurations to confirm symmetry.

the potential to be offset by the reduced Reynolds number of the scaled model compared to full scale, 6×10^5 and 1.7×10^7 respectively, as boundary layer thickness is inversely proportional to Reynolds number. Further, in full-scale, on average, the boundary layer is not expected to have the chance to develop along the full length of a train. Ambient crosswinds normal to the direction of the train's movement could effectively push the boundary layer off the surface, reducing the effective length the boundary layer is able to develop.
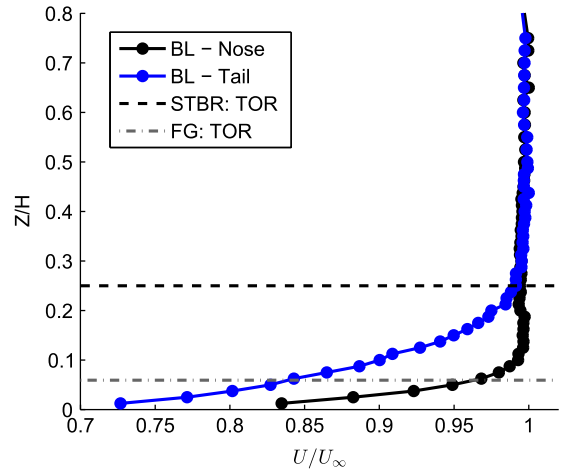

Fig. 6. Boundary layer velocity profile at nose (black) and tail (blue) position of the model over the splitter plate. Top of rail (TOR) for STBR and FG indicated by black and grey dotted lines respectively. $Z=0$ at splitter plate surface. (For interpretation of the references to colour in this figure caption, the reader is referred to the web version of this article.)

The development of the boundary layer over the roof of the scaled model is presented in Fig. 7, with both the momentum thickness and velocity profiles along the roof presented. The boundary layer over a HST has been shown to be highly three dimensional (Baker, 2010), with the side boundary layer being sensitive to distance above the ground. Thus the roof boundary layer was measured and analysed as a two-dimensional boundary layer for simplicity, as previous researchers have done (Baker, 2010; Muld et al., 2013a). The roof boundary layer on the simplified scale model is expected to be smaller compared to full-scale due to the large-scale roughness elements that exist on an operational full-scale train such as pantographs, heating, ventilation and air-conditioning (HVAC). As this experiment was performed with the focus on the influence of the train's external geometry on the air, no attempt to artificially manipulate the boundary layer, such as using additional ICGs (Muld et al., 2013a) or tripping was employed.

Momentum thickness was calculated using Eq. (2). The boundary layer profile was approximated using Eq. (3) from Munson et al. (2006) for the *z* values below those which were measurable ($z \leq 5$ mm):

$$\theta(x) = \int_0^\infty \frac{U}{U_\infty}\left(1 - \frac{U}{U_\infty}\right)dy, \tag{2}$$

$$U = U_\infty \left(\frac{y}{\delta}\right)^{1/7}, \tag{3}$$

$$\theta(x) = 0.0360 \left(\frac{\nu}{U_\infty}\right)^{1/5} x^{4/5}. \tag{4}$$

The momentum thickness between $x=0.1H$ and $x=0.2H$ in Fig. 7a remains small, due to accelerated flow over the nose, visible in the velocity profiles in Fig. 7b. Beyond $x=0.2H$, the momentum thickness is seen to grow over the length of the train. The development of the momentum thickness is greater at $y=0$ $(W/2)$ than at $y=0.25$ $(W/2)$.

Also shown in Fig. 7 is the estimated development of momentum thickness over the scaled model and a full-scale model, based on their respective freestream velocities (28 m/s and 83 m/s) and lengths (3.5 m and 200 m) using the flat plate approximation in Eq. (4) from Munson et al. (2006). This is the same approach taken in Muld et al. (2013a).
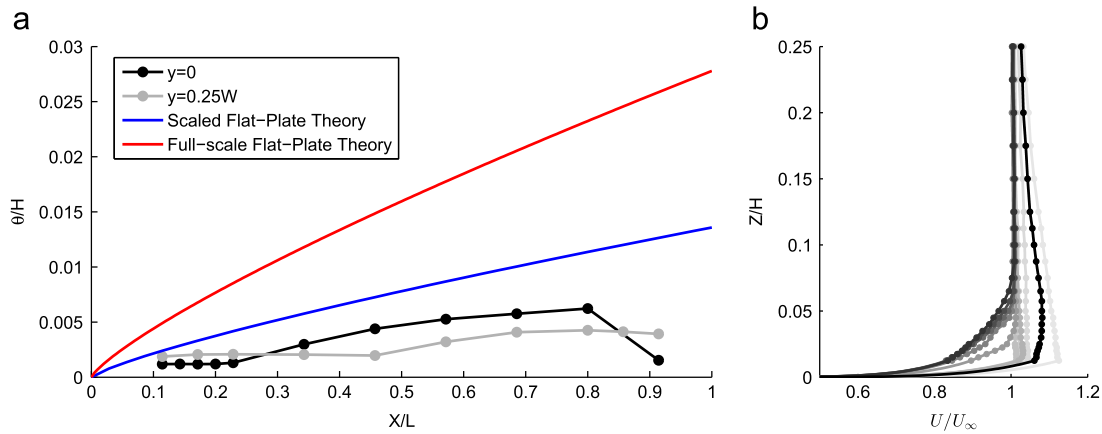
Fig. 7. (a) Development of the boundary layer momentum thickness over the length of the roof. Black: $y=0$ experimental data, grey: $y=0.25W$ experimental data, blue: scaled flat plate theory, and red: full-scale flat plate theory. (b) Experimental boundary layer profiles at $y=0$, $x=1$, 1.25, 1.5, 1.75, 2, 3, 4, 5, 6, 7, and $8H$ (light grey to dark grey respectively). (For interpretation of the references to colour in this figure caption, the reader is referred to the web version of this article.)

The scaled experimental boundary layer thickness develops to a momentum thickness of approximately 50% of the scaled (theoretical) approximation, and 17% of the full-scale momentum thickness approximation. The poor comparison between the scaled experimental and scaled flat plate approximation results reduces confidence that the full-scaled flat plate approximation is representative of a full-scale operational train, however, given the three-dimensional geometry, this is not surprising.

Specifically considering the height of the boundary layer development over the model, the reduced Reynolds number of the experiment is a potential benefit, due to the inverse relationship between boundary layer height and Reynolds number. Given the same L/H, an experiment with lower Reynolds number should develop a larger boundary layer than that for a full-scale train with a higher Reynolds number. However, the scaled model also has a reduced L/H. Comparison of the scaled to full-scale flat plate approximations in Fig. 7 show that the potential benefit of a reduced Reynolds number is outweighed by the reduced L/H.

A model with a smaller cross-sectional scale than tested would allow a larger L/H (given the same test section size) and also result in a lower Reynolds number, thus comparison between the scaled and full-scale flat plate approximations would be improved. However, the global flow topology may be more susceptible to varying from that at full-scale due to Reynolds number sensitivity, and, importantly, the ground boundary layer developing over the stationary floor would become larger relative to the model's height.

From these results it is likely that the boundary layer does not develop to a scaled equivalent of that expected on a full-scale, full length train. The consequences of this in terms of the resulting wake structure and slipstream however are not understood. Work by Muld et al. (2013a) has investigated the influence of L/H numerically, finding that no major flow structures changed between $L/H=12.5$, 19 and 25, however the dominant frequency was found to be sensitive to L/H. This is discussed further in Section 4.5.

2.4. Moving model experimental setup

Data from a separate moving model experiment (MME) was used to develop a methodology for performing gust analysis on data obtained from wind tunnel experiments. The MME experiment was performed at Deutsches Zentrum für Luft- und Raumfahrt (DLR - German Aerospace Centre) Tunnel Simulation Facility (TSG), a moving model facility in Göttingen, Germany. A moving model method has the advantage of measuring slipstream with the same train-measurement probe relative motion as full-scale field experiments.

A 1/25 scale model of an ICE3 – a HST in operation throughout Germany – was used. Two pairs of light gates were used to determine the models' velocity and acceleration, single hot wires were used to measure the induced velocity.

Three scenarios were tested: the primary scenario was a 3 car, 2.7 m long model fired at 32 m/s (Re=250,000, width as characteristic length), the reduced length scenario was a 2 car, 2.0 m long model ($L/H=12$) fired at 32 m/s and the maximum Reynolds number scenario was a 3 car, 2.7 m long model fired at 43 m/s (Re=330,000). Further details of the MME methodology and results are provided in Bell et al. (2014).

3. Analysis

3.1. Velocity

Full-scale field experiments assessing the slipstream of HSTs have been performed using ground-fixed probes, most commonly ultrasonic anemometers (Baker et al., 2012a,b). This data is obtained in the ground-fixed frame-of-reference (GF), the perspective of a stationary observer. The velocities measured by the cobra probe in the wind tunnel have a train-fixed frame-of-reference (TF). The component of the velocity in the x direction (u) was converted to GF and normalised against the local free-stream velocity using Eq. (5). The data obtainable in TF and GF methodologies, such as wind tunnels, and moving model or full-scale, respectively, is outlined in Fig. 8:

$$u_{GF} = 1 - \frac{u_{TF}}{u_L}. \tag{5}$$

The component of the velocity in the y direction (v) was normalised against the local freestream velocity (u_L). The resultant of the u_{GF} and v (see Eq. (6)) components of velocity (U) is presented in the results unless otherwise stated, as this 'horizontal velocity' presents the safety risk of instability to a person, whereas vertical velocity is proposed not to present a safety risk. This corresponds to the TSI (European Rail Agency, 2008) and EN (CEN European Standard, 2009). This horizontal velocity is herein referred to as the 'slipstream velocity':

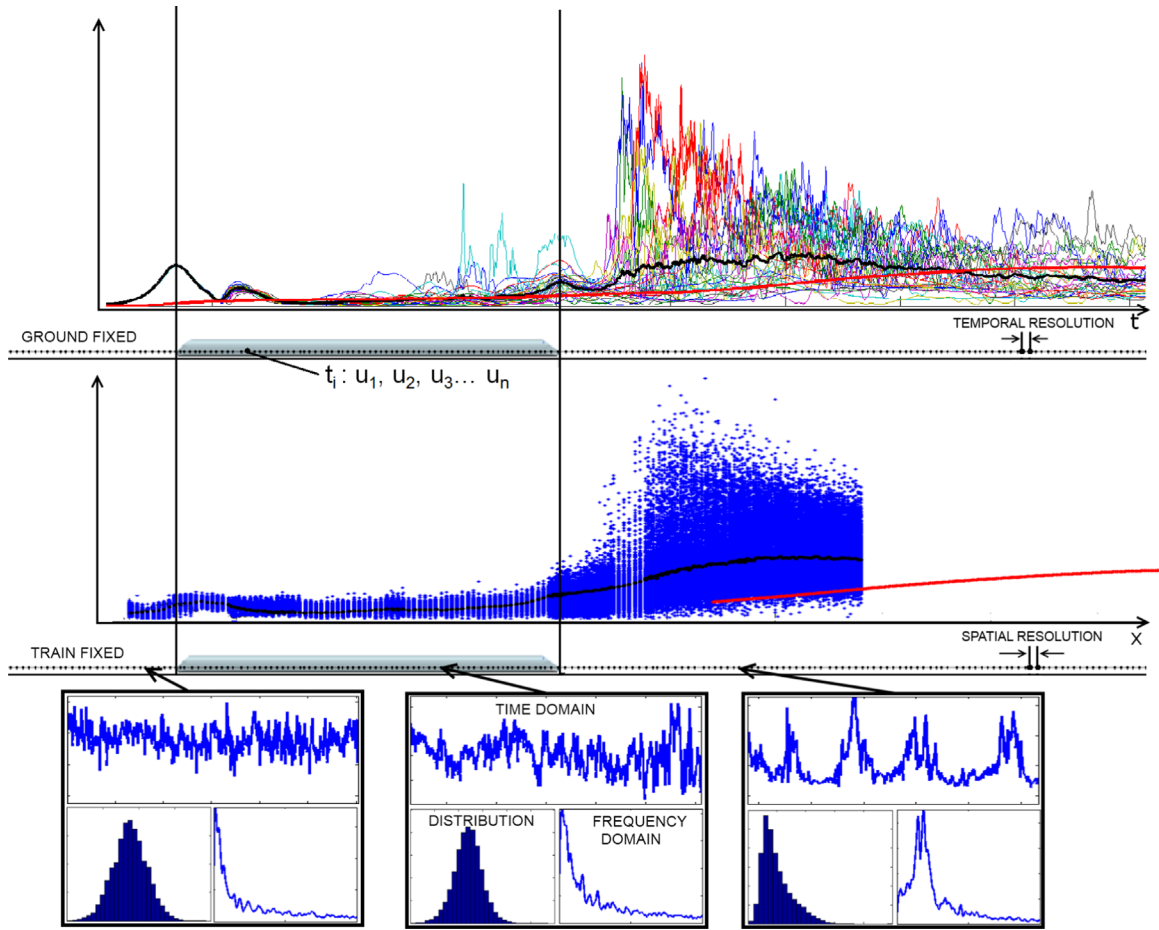$$U = \sqrt{u_{GF}^2 + v^2}. \tag{6}$$

Fig. 8. The data obtainable in the ground-fixed (GF) frame-of-reference (TOP) from a scaled moving model or full-scale field experiments, and train-fixed (TF) frame-of-reference (BOTTOM) from a wind tunnel experiment.

3.2. Slipstream profiles

The average slipstream velocity and standard deviation at each measurement position were calculated to develop the slipstream profiles presented in Section 4.1. These are equivalent to ensemble averages developed from individual runs of full-scale field tests or scaled moving model tests, where data is obtained in the ground-fixed frame-of-reference. An entire sweep of the streamwise slipstream profiles consisted of six physical positions in which the mechanical traverse was mounted to sweep the cobra probe. In some cases, this resulted in minor offsets of the calculated slipstream profile, believed to be due to small differences in the location of the cobra probe head in different traverse positions. The slipstream profiles were corrected by calculating the average offset between overlapping sections. The offsets applied were within $\pm\,0.01(U)$.

3.3. Gust

A HST's slipstream performance is characterised by a single value, the 'TSI value' in the TSI (European Rail Agency, 2008). The TSI value is calculated using Eq. (7), being the sum of the mean and two times the standard deviation of a data set comprised the maxima from each filtered (1 s moving average) individual run. The components that constitute the TSI value are illustrated in Fig. 9:

$$\text{TSI}_{GF} = \overline{U} + 2\sigma, \tag{7}$$

where $\overline{U}$ is the mean of the values in the data set: maxima from each filtered (1 s moving average) individual run and σ the standard deviation of the values in the data set: maxima from each filtered (1 s moving average) individual run.

An empirical method was developed to estimate the TSI_{GF} with a TSI_{TF}, a TSI value calculated from data obtained in the train-fixed frame-of-reference. First, GF data obtained from the moving model experiment (MME) outlined in Section 2.4 was used to calculate ensemble averages and ensemble standard deviations. It was assumed that a GF ensemble average and ensemble standard deviation is statistically equivalent to TF average and standard deviation profiles as depicted in Fig. 8. Thus, the ensemble average and ensemble standard deviation calculated from the MME could be used as TF equivalent data, and the method used to calculate a TSI value from TF data, TSI_{TF}, could be compared to the TSI_{GF} calculated from the same data, to assess the accuracy of the TSI_{TF} methodology.

To obtain the TSI_{TF}, a spatial moving average, equivalent to a 1 s moving average in full-scale, was applied to the ensemble averages and standard deviations, and the maxima of these were calculated. Thus the same components and processes were used as the TSI_{GF} calculation.

The final stage of the TSI_{TF} methodology was to add the maxima of the average profile (with a 1 s moving average applied) to 0.9 times the maxima of the standard deviation profile (with a 1 s moving average applied). The formula for estimating the TSI single value in a train-fixed frame-of-reference (TSI_{TF}) is provided as

$$\text{TSI}_{TF} = \max\left[(\overline{u}(x)_{1sMA} + 0.9\sigma(x)_{1sMA}\right], \tag{8}$$
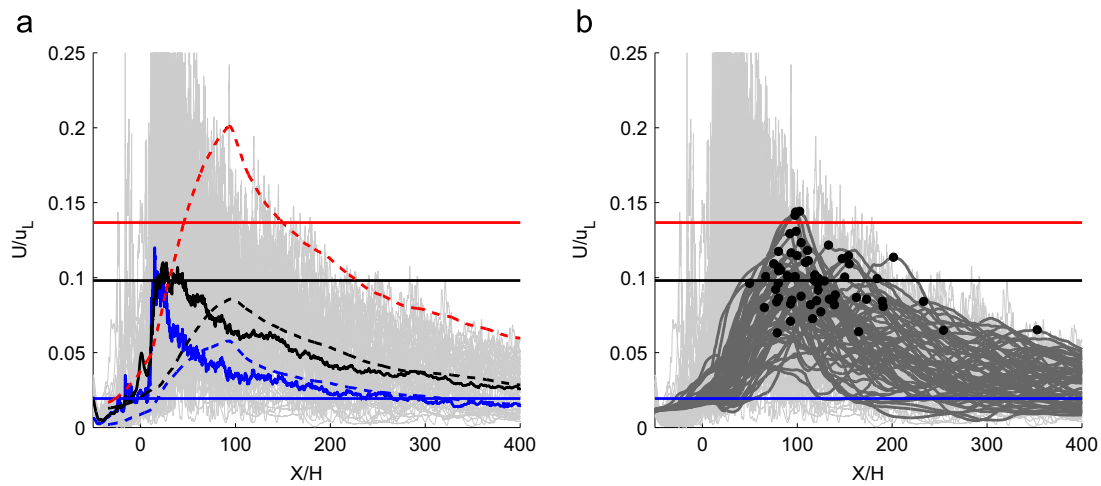
Fig. 9. (a). Data from a MME experiment (Bell et al., 2014) similar to that obtained in a wind tunnel, train-fixed frame-of-reference. Black: ensemble mean, dotted: 1sMA, blue: ensemble standard deviation, dotted: 1sMA, red: mean $+2$ standard deviation profile 1sMA. (b). Data obtained from ground fixed frame of reference – black points: maxima of each filtered individual runs (dark grey). Light grey: unfiltered individual runs. Horizontal red: TSI$_{GF}$ value, black: mean component, blue: standard deviation component. (For interpretation of the references to colour in this figure caption, the reader is referred to the web version of this article.)

where $\overline{u}(x)$ is the time average velocity at each position – with spatial moving average equivalent to 1 s moving average applied and $\sigma(x)$ the standard deviation of velocity at each position – with spatial moving average equivalent to 1 s moving average applied.

The empirical value of 0.9 when used to calculate TSI$_{TF}$ was consistent in estimating the TSI$_{GF}$ (within $\pm 3\%$) for three MME scenarios (varying length and Reynolds number). The explanation for the 0.9 factor multiplying the standard deviation instead of the more intuitive factor of 2, which is applied in the standard calculation of TSI$_{GF}$, is evident in Fig. 9. The maxima of the mean $+$ 2 standard deviation profiles (with 1sMA) in Fig. 9a significantly overestimate the TSI$_{GF}$, whose components are outlined in Fig. 9b. This is because the maximum of the ensemble standard deviation is almost twice that of the standard deviation of individual maxima. Also visible in Fig. 9a is that the maximum of the mean profile underestimates the mean of the maxima of the individual runs in Fig. 9b. A logical step to this simple, empirical approach would be to include two factors applied to the mean and standard deviation profiles separately to calculate TSI$_{TF}$, however no two common factors existed for the three MME scenarios analysed. Thus gust analysis was performed using the single factor of 0.9.

As the MME investigated a single geometry in three cases where length and Reynolds number were varied, the 0.9 factor has not been rigorously tested for sensitivity to the influence of geometry, or other factors such as Reynolds number and L/H, of which the influence on the slipstream profile and wake structure of HSTs remain unquantified. It is expected that a TSI$_{TF}$ based further in statistical or aerodynamic theory would be more robust to such changes, however, is yet to be developed. Thus, the 0.9 factor is used as a simplification to allow the estimation of TSI$_{GF}$.

The principal difficulty in applying gust analysis to TF type data is that no 'individual runs' exist for individual maxima to be determined from and then further processed to calculate a standard TSI value. Specifically, the difference in the type of correlation between the two data types as visible in Fig. 8. Data from the GF data is correlated in 'distance' (relative to the tail, either in time or space), however each individual run, and corresponding maxima is not correlated to any other. The TF data is correlated in time at each point in space measured (a time signal was obtained), but each measurement point is not correlated to another, as each was measured by a single probe, at different points in time.

The TSI$_{TF}$ ignores the correlation in time at each position in TF data, assuming zero correlation due to simplicity. This is the likely cause of the higher standard deviation measured in TF. Groups of values with specific magnitudes that are correlated in time (associated to a single turbulent structure) are not discounted with only the largest being considered. In comparison to GF gust analysis, one single maxima is obtained for each run.

3.4. Frequency and probability distribution

Analysis of the measurements taken at multiple positions along the length and in the wake of the vehicle was performed in the time and frequency domain in the form of probability distribution analysis, and power spectral density (PSD) analysis respectively. A Fast Fourier Transform (FFT) was utilised to convert to the frequency domain. A Hanning window methodology was applied, consisting of 3000 samples with a shift of 1500. The average of the multiple windows was then taken in an attempt to reduce spectral leakage. The PSD at each position was normalised by the maximum PSD of all the samples presented. The frequency was converted to Strouhal number, using the width of the model, 0.3 m as the characteristic length and freestream velocity (28 m/s) as characteristic velocity. The probability distribution of U is also presented. For displaying a segment of the U time signal, the real time was converted to non-dimensional time, using the freestream velocity (28 m/s) and model width (0.3 m).

4. Results

4.1. Slipstream profiles

The slipstream velocity profiles for both ground configurations can be seen in Fig. 10. The 'standard slipstream profile' is visible for both configurations and both heights measured, with peaks at the nose, tail, and the largest in the near wake. Due to test section length restrictions, a clear maximum was not obtained for the STBR platform height profile.

Comparing the STBR to the FG profiles, it should be noted that the track-side and platform heights are relative to the TOR, thus the FG measurements are closer to the stationary floor of the splitter plate, therefore expected to be under greater influence of the ground boundary layer. This would result in larger freestream
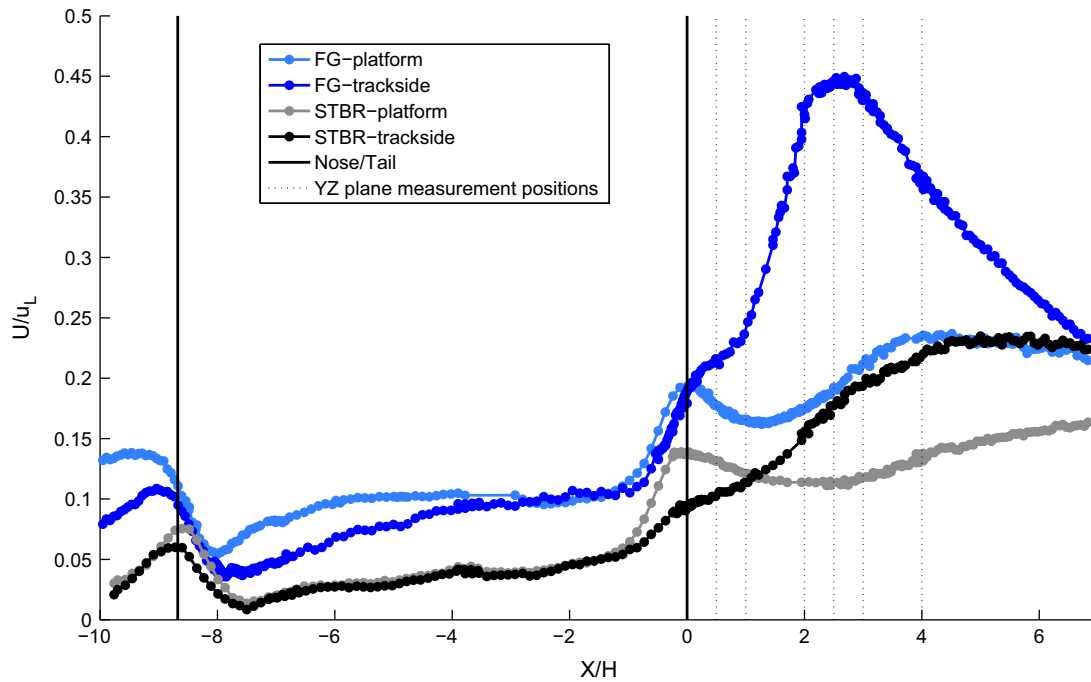
Fig. 10. Mean slipstream profiles U/U_L. Black: STBR – trackside, grey: STBR – platform, Blue: FG – trackside, Light-blue: FG – platform. Dotted lines: measurement positions of yz planes. (For interpretation of the references to colour in this figure caption, the reader is referred to the web version of this article.)

Table 1
Near wake peak slipstream magnitudes from other research.

Reference	Method	Scale	Re[a]	Track-side height			Platform height[d]		
				Peak[b]	y	z[c]	Peak[b]	y	z[c]
STBR	WT	1:25	6.0×10^5	0.23	2.0	0.05	0.15	2.0	0.35
FG	WT	1:25	6.0×10^5	0.45	2.0	0.05	0.25	2.0	0.35
Baker et al. (2001)	MME	1:25	2.5×10^5	–	–	–	0.09	2.0	0.5
Baker et al. (2012a)	Field	1:1	1.5×10^7	0.23	1.7	0.125	–	–	–
Gilbert et al. (2013)	MME	1:25	3.0×10^5	0.23	2.0	0.05	0.10	2.0	0.58
Sterling et al. (2008)	MME	1:25	2.5×10^5	0.21	1.7	0.125	0.05	1.7	0.56
Sterling et al. (2008)	Field	1:1	1.5×10^7	0.28	1.5	0.125	–	–	–
Sterling et al. (2008)	Field	1:1	1.5×10^7	0.18	2.1	0.125	–	–	–
Hemida et al. (2013)	CFD (LES)	1:20	3.0×10^5	0.31	1.3	0.05	0.19	1.33	0.39
Muld et al. (2013b)	CFD (DDES)	1:50	6.0×10^4	0.14	2.0	0.05	0.09	2.0	0.35

[a] Reynolds number is estimated using scale to obtain width, train/freestream velocity and kinematic viscosity of air at 15 °C : 1.46×10^{-5} kg/m²/s if not stated.
[b] Peak magnitudes are estimates from visual inspection of figures in the referenced literature.
[c] Positions provided are above top of rail (TOR), normalised by height.
[d] Platform height was without a physical platform in all cases except for Muld et al. (2013b).

velocity deficit, which when converted to the ground-fixed frame of reference corresponds to a larger induced velocity. This is evident in the nose peak, where FG exhibits a greater magnitude than the STBR at both heights. Further, the FG results consistently exhibit larger slipstream velocity than STBR, with a much sharper and earlier near wake peak at track-side height.

The ground boundary layer is a deficit in freestream velocity. The frame of reference calculation would interpret this deficit as slipstream velocity (Eq. (5)). Thus, as the ground boundary layer grows the further from the splitter plate leading edge, the velocity deficit would increase, and one would expect to see a slipstream profile that continues to increase with distance from the splitter plate leading edge. However, the FG track-side profile in Fig. 10 clearly shows a near wake peak at $X=3H$. This is a strong indicator that the profile is dominated by the near wake of the train

generated by the train geometry and not the ground boundary layer.

The magnitudes of the near wake peaks for the STBR track-side and platform heights (0.225 and 0.150 respectively) are within the range of slipstream magnitudes for an ICE2 train found by other researchers provided in Table 1. Full scale results themselves are susceptible to significant differences in peak magnitudes between experiments (Baker et al., 2012a; Sterling et al., 2008).

The platform height having a lower magnitude peak than the track-side height is also consistent with full-scale results (Baker, 2010; Baker et al., 2012a; Sterling et al., 2008). However, the magnitudes of the slipstream peaks calculated with FG (0.45 and 0.25) are far greater than all others found in the literature at both measurement heights. As the STBR ground configuration compares better to the limited full-scale results available, it is proposed that
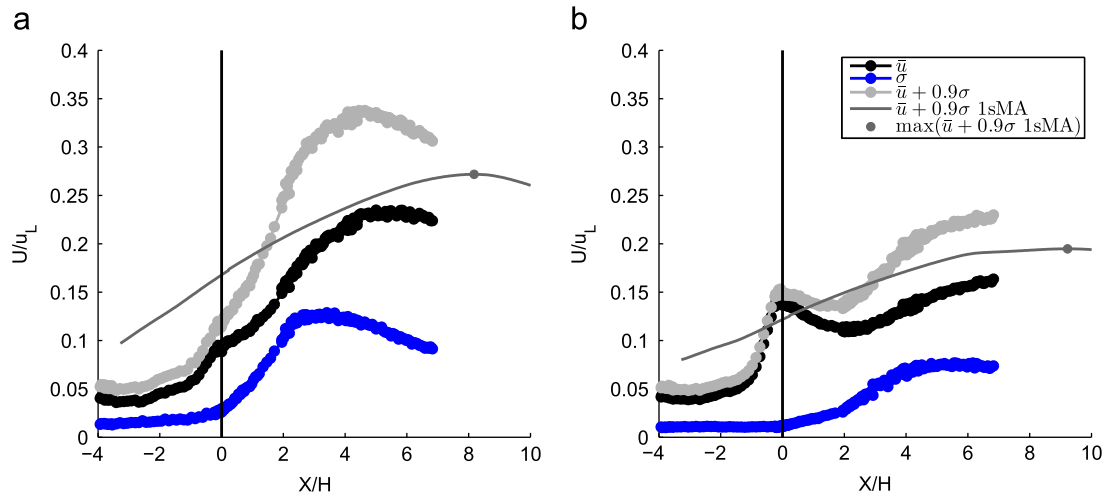
Fig. 11. Slipstream profiles, STBR ground configuration U/U_L: (a) track-side, (b) platform measurement position. Black: mean, grey: mean + 0.9 standard deviations, blue: standard deviation. Grey line = spatial average equivalent to full-scale 1 s moving average of mean + 0.9 standard deviations, maxima indicated by point. (For interpretation of the references to colour in this figure caption, the reader is referred to the web version of this article.)

the STBR is a better representation of the ground configuration and frequency, distribution and gust results presented focus on this configuration.

A significant difference between the results with those at full-scale is the location of the near wake peak, which is much closer to the tail for both ground configurations at 2.5*H* and 5*H* for the FG and STBR respectively. Following the near wake peak, it is expected that the slipstream profile decays with a power law profile as found by Baker et al. (2012a). Full-scale results show peaks to be approximately 7–15*H* from the tail (Baker et al., 2012a; Sterling et al., 2008). A possible explanation for this difference is the idealised conditions (zero ambient wind) in these experiments, where exposure to ambient wind in full-scale could diffuse the flow structures causing the near wake peak.

Other researchers who have investigated slipstream in the ground-fixed frame-of-reference have found significant run-to-run variation, specifically in the near wake (Baker et al., 2012a,b; Sterling et al., 2008). This is also illustrated in the experimental results presented in Fig. 11a and b, which show peaks in standard deviation in the near wake for the STBR at both measurement positions. The maximum standard deviations in Fig. 11 are 0.14 and 0.08 for track-side and platform respectively. Similar results in the train-fixed frame-of-reference were also predicted numerically by Hemida et al. (2013) with turbulence intensity of 13–16% in the near wake, whilst all other locations contained at largest 10–12%.

4.2. Reynolds number sensitivity

A full-scale train travelling at 300 km/h has a Reynolds number of 17×10^6 with width as the characteristic length. This is significantly larger than was achievable in the experiment. Thus, sensitivity of the results to Reynolds number over the range 4×10^5–7×10^5 – corresponding to freestream velocities of 20–37 m/s – is presented.

The sensitivity of the longitudinal slipstream profiles to Reynolds number is presented in Fig. 12. It can be seen that for both the STBR and FG configurations (at track-side position) that the lowest Reynolds number (4×10^5 ($U_f = 20$ m/s)) is different to the two higher Reynolds numbers tested at 6×10^5 ($U_f = 30$ m/s) and 7×10^5 ($U_f = 36$ m/s). In both cases this results in a lower normalised near wake peak. The differences between two higher Reynolds number profiles are negligible and fall within the experimental error.
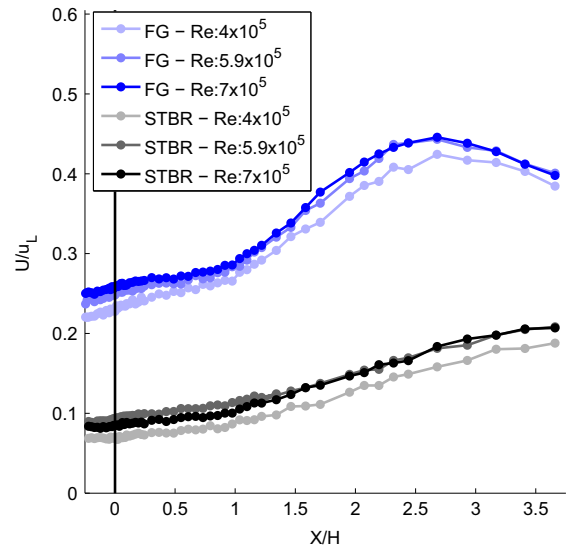

Fig. 12. Reynolds number sensitivity. *yz* longitudinal U/U_L profiles.

The EN recommends scaled high-speed train slipstream testing to be performed at a Reynolds number greater than 2.5×10^5 (CEN European Standard, 2009) however the generally accepted value of the critical Reynolds number for ground vehicles is 1×10^6, beyond which flow structure is not expected to change significantly. In Section 2.3 it is apparent that a lower Reynolds number is beneficial in terms of the development of a realistic relative boundary layer. Hence the Reynolds number has a trade-off relationship. Results presented herein have a Reynolds number of 6×10^5 unless stated otherwise.

4.3. Gust

The TSI_{TF} single values calculated using the methodology outlined in Section 3.3 for the STBR track-side and platform heights were 0.272 and 0.195 respectively (see Fig. 11). Full-scale TSI values of an ICE2 at similar track-side and platform measurement positions fall within the range of 0.269–0.280 and 0.177–0.220 respectively (Baker et al., 2012b). Similar to the slipstream profiles, this gust analysis compares well to full-scale results.
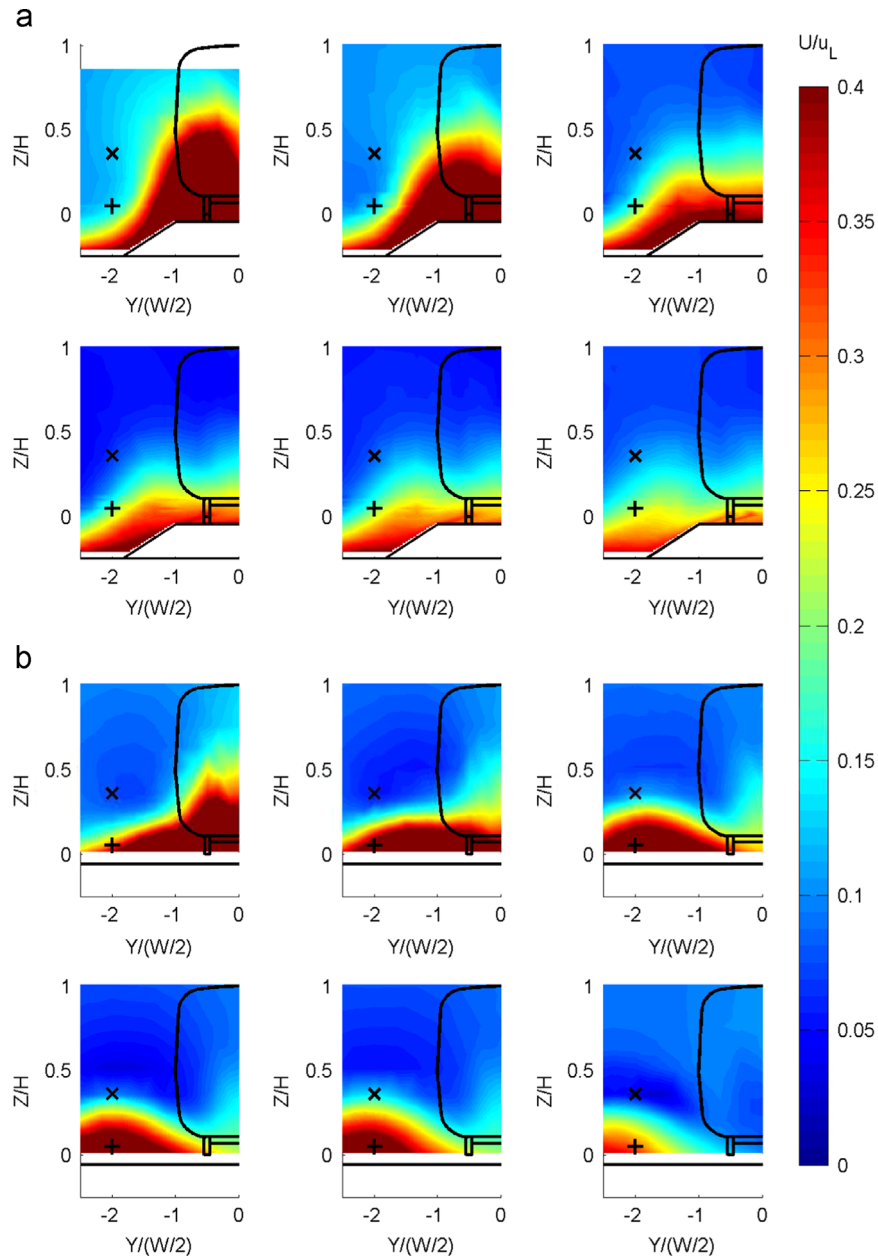
Fig. 13. yz wake profiles of U/U_L. The vortex can be seen to move downwards and outwards across the path of the two track-side ($+$) and platform ($\times$) longitudinal measurement positions for both ground configurations. (a) STBR and (b) FG. Top, left to right: $x=0.5$, 1, $2H$. Bottom, left to right $x=2.5$, 3, $4H$.

4.4. Flow structure

The time averaged results presented in Figs. 13–15 indicate that the near wake slipstream peaks evident in Fig. 10 are explained by a pair of streamwise counter-rotating vortices.

Contours of the slipstream velocity, U, are included directly in Fig. 13 for both ground configurations, at each of the 6 yz planes measured. Vorticity, Γ_2 (vortex boundary defined as $\Gamma_2 = 2/\pi$, vortex core defined as the maxima of Γ_1, and the v,w components of velocity these quantities are derived from, are presented in Fig. 14. These parameters are commonly used to define a coherent vortex (Graftieaux et al., 2001; Jeong and Hussain, 1995). Both Figs. 13 and 14 indicate the presence of a time average vortex that moves downwards and outwards. This lateral movement of these counter-rotating longitudinal vortices is consistent with inviscid flow theory, where no flow through the ground can be represented by mirror images of each of the vortices. The self-induction of the vortex pair and interaction with the image pair causes the pair to move initially towards the ground and then away from each other. As the pair approach the ground, some level of flattening of the cores occurs (Westphal and Mehta, 1989; Pauley and Eaton, 1988; Lödgberg et al., 2009). In this case it is the no-slip condition in the spanwise direction that causes this lateral movement, and the no-slip condition in the streamwise direction, from the artificially imposed stationary floor, is not expected to influence this motion significantly.

The three-dimensional data presented in Fig. 15 was created from interpolating between the 6 yz planes measured with the cobra probe. The vortex is identified using the quantity of Γ_2 (Michard et al., 1997; Graftieaux et al., 2001) and the condition that $\Gamma_2 = 2/\pi$ defines a vortex (Graftieaux et al., 2001) (plotted as the iso-surface in Fig. 15). The intensity of the vortex in terms of induced velocity (denoted as the colour of the iso-surface in Fig. 15) reduces as it moves away from the tail.
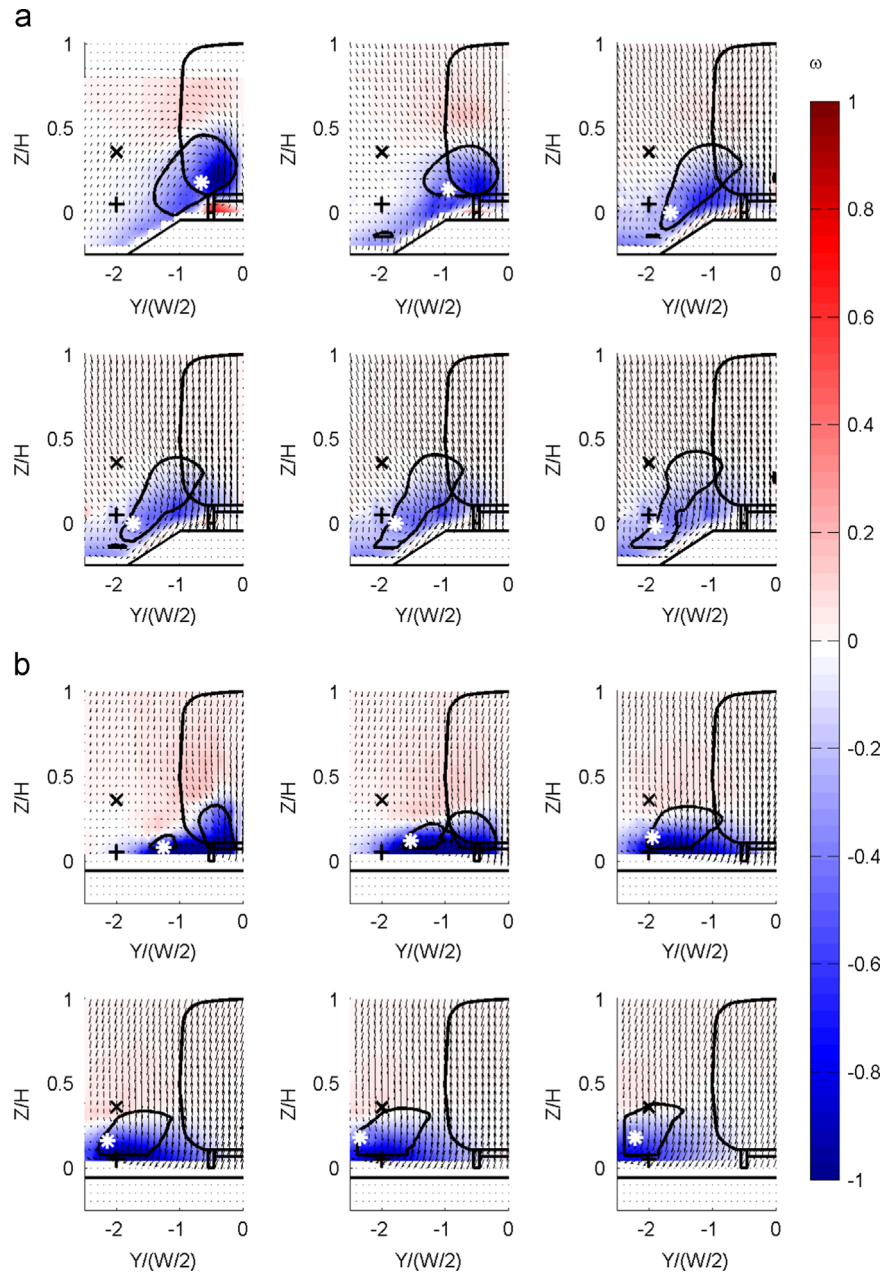
Fig. 14. yz wake profiles of vorticity, overlaid with v/U_L, w/U_L, velocity vectors. Black contour line: $\Gamma_2 = 2/\pi$, $* = \Gamma_{1MAX}$. The vortex can be seen to move downwards and outwards across the path of the two track-side ($+$) and platform ($\times$) longitudinal measurement positions. (a) STBR and (b) FG. Top, left to right: $x = 0.5$, 1, 2H. Bottom, left to right $x = 2.5$, 3, 4H.

The presence of a pair of streamwise counter-rotating vortices has been identified in previous research (Baker, 2010; Hemida et al., 2013; Weise et al., 2006; Muld et al., 2012; Yao et al., 2013) in time averaged flow, which move from directly behind the tail, downwards and outwards. Whether these structures exist in transient flow, and if they do, how they exist has not been explicitly identified in previous research. However, work by Heine et al. (2013) in the same experimental setup described in Section 2.4, with the addition of high-speed Particle Image Velocimetry (PIV), did observe a coherent streamwise vortex in the transient flow behind the scaled ICE3 model.

It is expected that the dual cores visible close to the tail in FG configuration in Figs. 15 and 14b occur due to the difficulty in calculating Γ_2 close to a boundary, in this case the ground, rather than representing two separate coherent structures.

The differences in the slipstream profiles between the two ground configurations evident in Fig. 10 are explained in Figs. 13–15, which show significantly different wake structures. The vortex moves outwards much earlier in the FG configuration compared to the STBR. The core of the vortex also travels directly across the longitudinal slipstream measurement positions for the FG configuration. For the STBR, the vortex core moves partially underneath the slipstream measurement position due to the ballast shoulder and increased distance of the measurement positions to the ground. This explains the higher magnitude slipstream peak that is closer to the tail and dissipates more rapidly in FG than STBR configuration.

As discussed in Section 4.1, the ground boundary layer is a deficit in the freestream velocity and is interpreted as slipstream velocity through the conversion to the GF frame-of-reference in
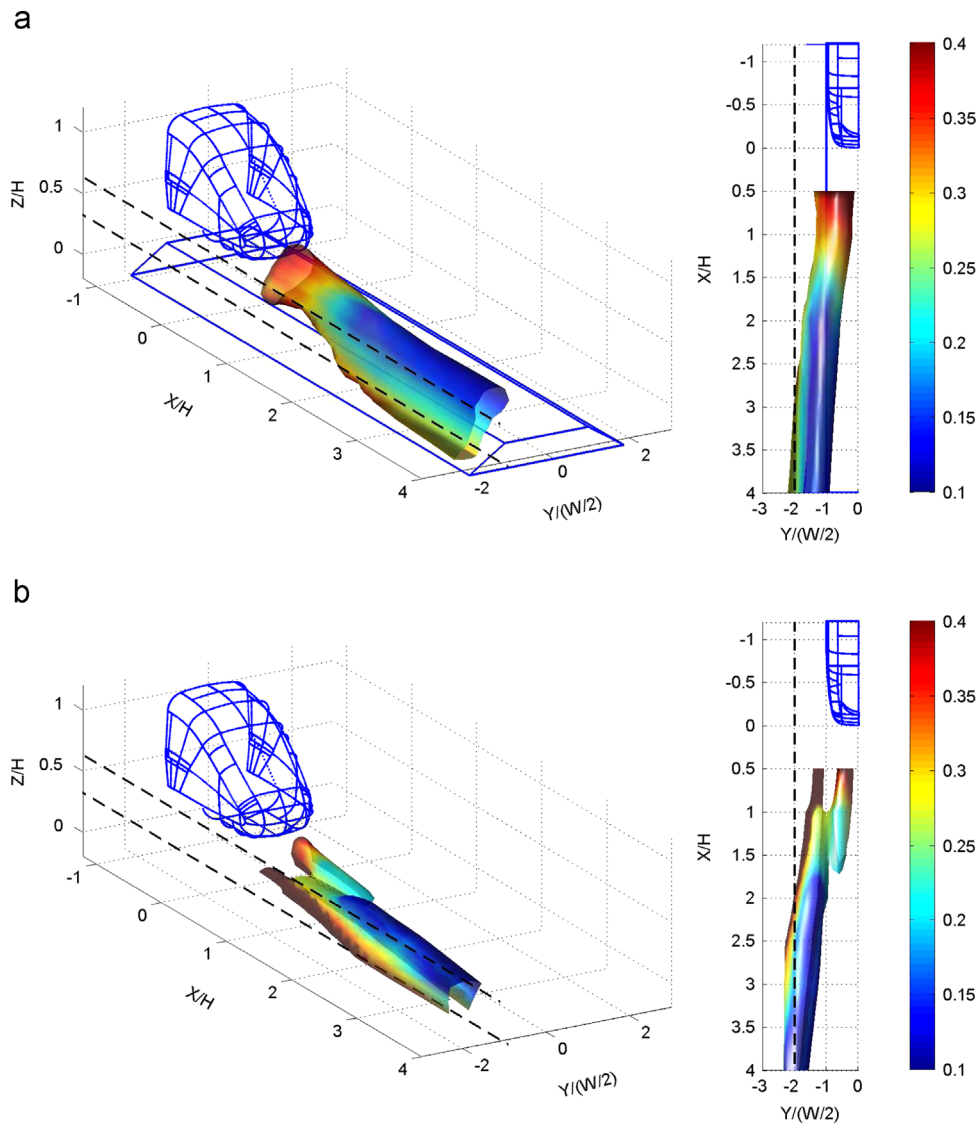
Fig. 15. Three-dimensional isosurfaces of $\Gamma_2 = 2/\pi$, denoting time averaged vortex in the wake. Surface colour is slipstream magnitude. Black dotted lines=TSI track-side and platform measurement positions corresponding to longitudinal slipstream profiles presented above. (a) STBR and (b) FG. Three-dimensional data obtained from interpolation of 6 *yz* planes presented below. (For interpretation of the references to colour in this figure caption, the reader is referred to the web version of this article.)

Eq. (5). However, the ground boundary layer in the wake is not well defined for either ground configuration in Fig. 13. From results presented in Section 2.3, Fig. 6, if the boundary layer was dominant, there would be a horizontal band of slipstream velocity visible. It appears that the wake structure resulting from the flow around the tail is the dominant feature, and effectively washes away the majority of the boundary layer.

Thus, from the lack of boundary layer influence on the YZ contour slices and the clear near wake peaks in slipstream profiles as discussed in Section 4.1, it does not appear that the ground boundary layer significantly contributed to the slipstream profiles presented in Section 4.1.

Although the boundary layer is not clearly dominating the measurements, the presence of the stationary floor presents different flow conditions and the wake structure is expected to show differences to a moving floor setup. It is believed that the stationary floor results in an increased flattening of the overall wake structure. This is a common finding for longitudinal vortices embedded in or moving towards a boundary layer (Westphal and Mehta, 1989; Pauley and Eaton, 1988; Lödgberg et al., 2009). The distortion of the ground boundary layer by a vortex leads to rapid diffusion of streamwise vorticity resulting in the growth of

the vortex core (Pauley and Eaton, 1988), which increases the flattening of the core, discussed above (Westphal and Mehta, 1989; Lödgberg et al., 2009). The implication of this is that the measurement heights may not be consistent in position relative to the wake structure between the two different setups. This is less of a problem for low measurement heights, such as the track-side measurement position, where the vortex core passes through it regardless of minor changes in *z* position, but is potentially more important for higher measurement positions, such as the platform height, which is closer to the edge of the vortex, and thus slipstream results may be more sensitive to minor changes in measurement height.

These slipstream and flow structure results have two important implications. The first is that the ground configuration modelled, at least with a stationary floor setup as in wind tunnel experiments, has a significant effect on the wake structure and resulting slipstream profile. Secondly, in spite of the stationary floor and resulting ground boundary layer, the general wake structure, as identified by other researchers (Baker, 2010; Hemida et al., 2013; Weise et al., 2006; Muld et al., 2012; Heine et al., 2013), has been established, and these results are indicated to be responsible for the slipstream profiles characteristic near wake peak found in
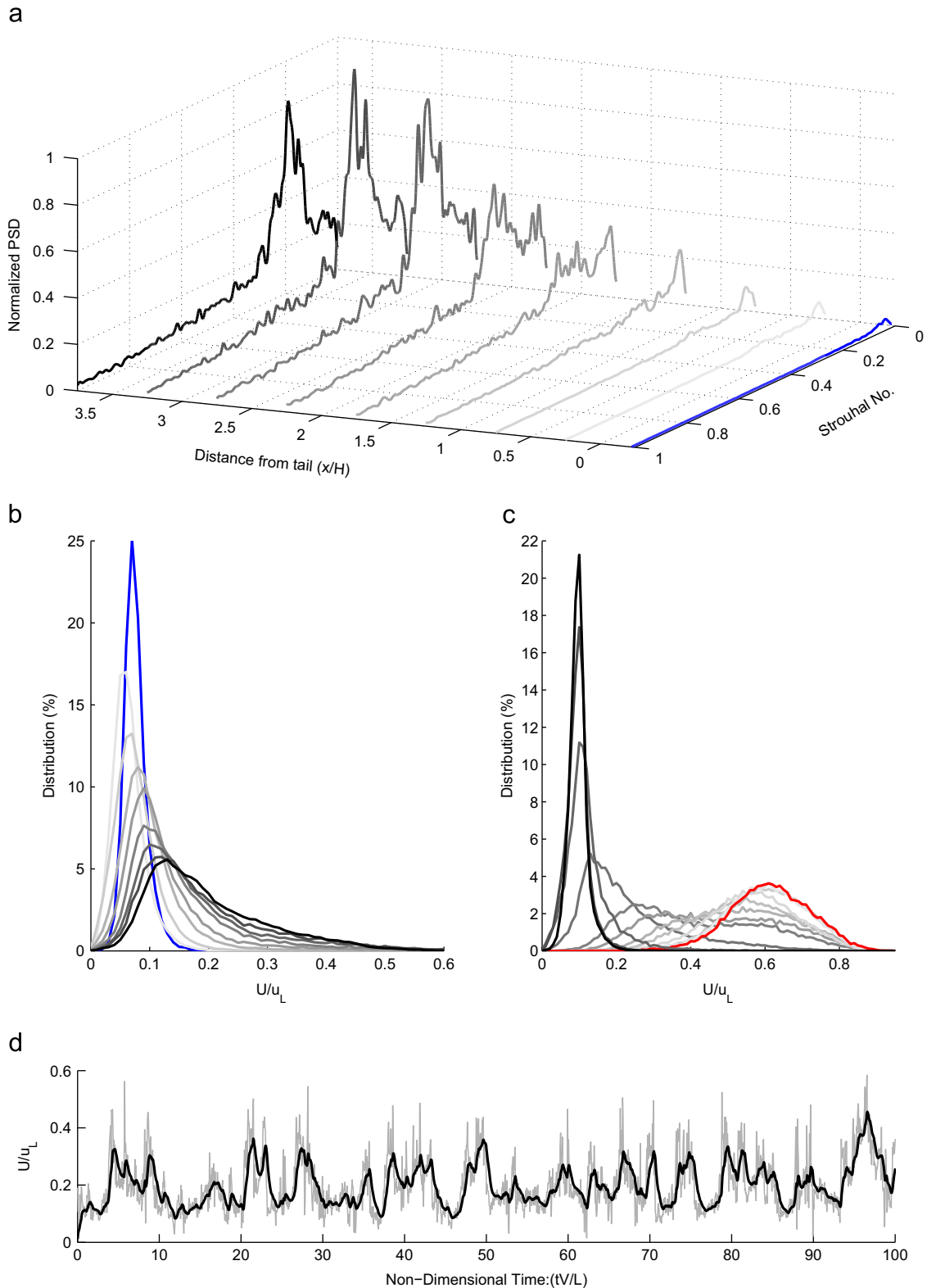
Fig. 16. Streamwise development of (a) normalised power spectral density and (b) distribution of U/u_L at $x = -0.25H$ (blue), $0.25H$, $0.75H$, $1H$, $2.25H$, $2.75H$, $3.25H$, $3.75H$ (increasing darkness), $y = 2(W/2)$, $z = 0.05H$ ATOR (TSI track-side position). (c) Spanwise development of probability distribution of U/u_L at $y = 0$ (red), 0.16, 0.33, 0.67, 0.83, 1, 1.16, 1.33, 1.67, 2, 2.33, 2.67 $(W/2)$, $x = 1H$, $z = 0.005H$ (increasing darkness). (d) Time signal of U/u_L at $x = 1H$, $y = 2(W/2)$, $z = 0.05H$. (For interpretation of the references to colour in this figure caption, the reader is referred to the web version of this article.)

scaled experimental (Baker, 2010; Sterling et al., 2008; Bell et al., 2014; Gilbert et al., 2013), numerical (Muld et al., 2013b; Hemida et al., 2013), and full-scale experiments (Baker, 2010; Baker et al., 2012a,b; Sterling et al., 2008) alike.

4.5. Frequency and probability distribution

Investigations into the transient nature of the wake structure are presented here in an attempt to provide insight into the large

run-to-run variations visible in full-scale and scaled moving model slipstream results (Baker, 2010; Baker et al., 2012a; Sterling et al., 2008; Bell et al., 2014; Hemida et al., 2013; Schulte-Werning et al., 2001). This is also indicated from the high standard deviation in the near-wake presented in Section 4.1 and Fig. 11.

The frequency spectra, probability distribution and time series are presented in Fig. 16a and b for multiple streamwise measurement points corresponding to the track-side position moving from the tail to the far wake. These results show an increasing prominence of a dominant frequency with a Strouhal number of ≈ 0.18 moving further into the wake. This corresponds to the increasing streamwise slipstream velocity in Fig. 10.

Previous researchers have also identified dominant frequencies in the near wake region of an ICE2 train. Baker (2010) presented analysis of the full-scale experimental data from Sterling et al. (2008) which identified a dominant frequency of St=0.11.

Schulte-Werning et al. (2003) using the Unsteady Reynolds Averaged Navier–Stokes numerical method, obtained instantaneous skin friction on the tail surface of an ICE2 that showed a spanwise oscillation of points of origin for two vortices, with a Strouhal number of 0.14.

Numerical research by Muld et al. (2012) using the Delayed Detached-Eddy Simulation (DDES) numerical method identified spanwise oscillations of a counter-rotating vortex pair, with a Strouhal number of 0.13. Further work by Muld et al. (2013a) predicted that the length of the train modelled influenced the dominant frequency, with trains having L/H of 12.5, 19, and 25 (2, 3 and 4 carriages) having dominant frequencies of 0.13, 0.095 and 0.085, respectively.

An explanation for the results in Muld et al. (2013a) and the variation in dominant frequencies found by Sterling et al. (2008), Schulte-Werning et al. (2003), and Muld et al. (2012) is the difference in boundary layer development. If the displacement thickness is added to the standard characteristic length, in this case width or hydraulic diameter, this would result in an 'effective' characteristic length. This effective characteristic length could be used to normalise the dominant frequency and hence calculate something similar to the 'universal' Strouhal number (Roshko, 1955). Thus, the different dominant frequencies found by previous researchers are potentially describing the same flow features.

Moving in the streamwise direction away from the tail, the probability distribution of slipstream velocity changes from a normal type distribution, with high kurtosis and low skewness to decreasing kurtosis and increasing positive skewness moving away from the tail into the wake (Fig. 16b). Skewed distributions such as these are common for high pressure fluctuations in the shear layer and separation region of bluff bodies (Letchford et al., 1993; Ginger and Letchford, 1993). The segment of time series measured at $x=3.5H$, $y=-2(W/2)$m $z=0.05H$ in Fig. 16d also indicates a periodic nature, made clearer with a 40 Hz low-pass filter.

The difference in probability distribution moving in the spanwise direction from directly behind the model ($y=0$) to beyond the TSI measurement line ($y=-4$) at $x=1H$ is presented in Fig. 16c. The probability distribution transitions from a normal like distribution with medium kurtosis and low skewness to gradual increasing skewness, at the point where two modes are visible (with one side still being more dominant) before moving into the highly skewed distribution near the TSI line ($y=-2(W/2)$) and high kurtosis and low skewness further from the centre.

The results in this section associate the high time-averaged slipstream velocities, evident in both longitudinal slipstream profiles and wake slices, to periodic features within the wake, explaining the high standard deviation in these areas. Further analysis is required to define the transient nature of the flow that is responsible. However, the importance of the transient flow is evident from these results.

5. Conclusions

An experimental investigation into the slipstream of a high-speed train through flow mapping in the wake and streamwise measurements with dynamic pressure probes has been presented.

The scale model wind tunnel methodology was able to identify the 'standard slipstream profile', specifically the peak in slipstream magnitude in the near-wake, as found by previous research in scaled, numerical and full-scale investigations. The flow mapping performed associated this near-wake peak in slipstream velocity to one of a pair of counter rotating vortices that move outwards from the tail. Thus, the advantage of a wind tunnel approach and the train-fixed frame-of-reference, the ability to quantify the main wake flow features and identify the cause of slipstream characteristics, was successfully demonstrated.

The association between the longitudinal vortex pair and the slipstream peak existed for the two ground configurations considered: true flat ground and single track ballast and rail. However, features of the flow structure and resulting slipstreams were significantly different between the two. Each vortex of the pair moved outwards and over the longitudinal measurement position more quickly and in greater intensity for the flat ground relative to the single track ballast and rail configuration.

The measured slipstream magnitudes of the near-wake peaks at both streamwise measurement heights for the STBR (0.23, 0.15) case fell within the wide range of scaled, numerical and full-scale results from previous research on the same high-speed train geometry (0.14–0.31, 0.09–0.19), whilst for the FG (0.45, 0.25) was significantly higher.

The first iteration of a method for performing gust analysis, estimating the TSI single value, in the train-fixed frame-of-reference has been applied. Future iterations to the methodology should aim to remove its empirical nature. The estimated TSI values with the STBR ground configuration (0.272, 0.196) are again within the range of available full-scale results in the literature (0.269–0.280, 0.177–0.220).

The high run-to-run variation found in full-scale results was investigated with the analysis of velocity in the time and frequency domain measured experimentally. The high slipstream velocities and time-averaged vorticity in the time-averaged near-wake were further associated to quasi-periodic flow with highly skewed probability distributions. These results indicate the high run-to-run variance at full-scale might be attributed to capturing different phases of periodic flow of the trailing vortex pair. The work presented here aids the explicit identification of the flow mechanisms responsible for these transient results and thus improves the understanding of the slipstream and wake structure of a high-speed train.

The sensitivity of the slipstream results to wind tunnel experimental limitations: the reduced length of the model, the presence of a static floor and the reduced Reynolds number are yet to be quantified and this investigation is on-going.

In spite of the experimental limitations, the strength in quantitative comparison to full-scale results and strong qualitative comparison to wake structure and dynamics in the literature studies together suggest that the findings of this work are representative of the slipstream around full-scale high-speed trains. This work represents a step towards providing a consistent scaled wind tunnel methodology for assessing the slipstream risk of a prototype HST, as well as an improvement in the understanding of the flow structures underlying the slipstream effects for optimisation and risk mitigation of future high-speed trains.

Appendix A. Supplementary data

Supplementary data associated with this article can be found in the online version at http://dx.doi.org/10.1016/j.jweia.2014.09.004.

References

Ahmed, S.R., 1983. Influence on base slant on the wake structure and drag of road vehicles. J. Fluids Eng. Trans. ASME 105 (4), 429–434.

Baker, C.J., 2010. The flow around high speed trains. J. Wind Eng. Ind. Aerodyn. 98, 277–298.

Baker, C.J., Dalley, S.J., Johnson, T., Quinn, A., Wright, N.G., 2001. The slipstream and wake of a high-speed train. J. Rail Rapid Transit 215 (2), 83–99.

Baker, C., Quinn, A., Sima, M., Hoefener, L., Licciardello, R., 2012a. Full scale measurement and analysis of train slipstreams and wakes: Part 1: ensemble averages. Proc. Inst. Mech. Eng. Part F: J. Rail Rapid Transp. 98, 277–298.

Baker, C., Quinn, A., Sima, M., Hoefener, L., Licciardello, R., 2012b. Full scale measurement and analysis of train slipstreams and wakes: Part 2: gust analysis. Proc. Inst. Mech. Eng. Part F: J. Rail Rapid Transp. 98, 277–298.

Bearman, P.W., Beer, D.D., Hamidy, E., Harvey, J.K., 1988. The Effect of a Moving Floor on Wind-Tunnel Simulation of Road Vehicles. SAE Technical Paper No. 880245.

Bell, J.R., Burton, D., Thompson, M.C., Herbst, A.H., Sheridan, J., 2014. Moving model analysis of the slipstream ad wake of a high-speed train. Journal of Wind Engineering and Industrial Aerodynamics, submitted for publication (INDAER-D-14-00217R1), June.

CEN European Standard, 2009. Railway Applications – Aerodynamics. Part 4: Requirements and Test Procedures for Aerodynamics on Open Track, CEN EN 14067-4.

CEN European Standard, 2010. Railway Applications – Aerodynamics. Part 6: Requirements and Test Procedures for Cross Wind Assessment, CEN EN 14067-6.

CEN European Standard, 2013. Railway Applications – Aerodynamics. Part 4: Requirements and Test Procedures for Aerodynamics on Open Track, CEN EN 14067-4.

Choi, H., Lee, J., Park, H., 2014. Aerodynamics of heavy vehicles. Annu. Rev. Fluid Mech. 46, 441–4468.

European Rail Agency (ERA), 2008. EU Technical Specification For Interoperability Relating to the GÇRolling Stock Sub-System of the Trans-European High-Speed Rail System (HS RST TSI). 232/EC.

Gilbert, T., Baker, C.J., Quinn, A., 2013. Gusts caused by high-speed trains in confined spaces and tunnels. J. Wind Eng. Ind. Aerodyn. 121, 39–48.

Ginger, J.D., Letchford, C.W., 1993. Characteristics of large pressures in regions of flow separation. J. Wind Eng. Ind. Aerodyn. 49, 301–310.

Graftieaux, L., Michard, M., Grosjean, N., 2001. Combining piv, pod and vortex identification algorithms for the study of unsteady turbulent swirling flows. Meas. Sci. Technol. 12, 1422–1429.

Heine, D., Lauenroth, G., Haff, J., Huntgeburth, S., Ehrenfried, K., 2013. High-speed particle image velocimetry on a moing train model. In: Second International Symposium on Rail Aerodynamics, Berlin, Germany.

Hemida, H., Baker, C.J., Gao, G., 2013. The calculation of train slipstreams using large-eddy simulation. Proc. Inst. Mech. Eng. Part F: J. Rail Rapid Transp. 228, 25–36.

Hooper, J.D., Musgrove, A.R., 1997. Reynolds stress, mean velocity, and dynamic static pressure measurement by a four-hole pressure probe. Exp. Therm. Fluid Sci. 15, 375–383.

Jeong, J., Hussain, F., 1995. On the identification of a vortex. J. Fluid Mech. 285, 69–94.

Krajnović, S., Davidson, L., 2005. Influence of floor motions in wind tunnels on the aerodynamics of road vehicles. J. Wind Eng. Ind. Aerodyn. 93, 677–696.

Kwon, H., Park, Y., Lee, D., Kim, M., 2001. Wind tunnel experiments on Korean high-speed trains using various ground simulation techniques. J. Wind Eng. Ind. Aerodyn. 89, 1179–1195.

Letchford, C.W., Iverson, R.E., McDonald, J.R., 1993. The application of quasi-steady theory to full scale measurements on the Texas tech buidling. J. Wind Eng. Ind. Aerodyn. 48, 111–132.

Lödgberg, O., Fransson, J.H.M., Alfredsson, P.H., 2009. Streamwise evolution of longitudinal vortices in a turbulent boundary layer. J. Fluid Mech. 623.

Michard, M., Graftieaux, L., Lollini, L., Grosjean, N., 1997. Identification of vortical structures by a non local criterion: application to piv measurements and dns-les results of turbulent rotating flows. In: 11th Symposium on Turbulent Shear Flows, Grenoble, France, 25–30.

Morel, T., 1980. Effect of base slant on flow in the near wake of an axisymmetric cylinder. Aeronaut. Q., 132–147.

Muld, T., Efraimsson, G., Hennigson, D.S., 2012. Flow structures around a high-speed train extracted using proper orthogonal decomposition and dynamic mode decomposition. J. Rail Rapid Transit 57, 87–97.

Muld, T., Efraimsson, G., Hennigson, D.S., 2013a. Wake characteristics of high-speed trains with different lengths. J. Rail Rapid Transit. 228 (4), 333–342. http://dx.doi.org/10.1177/0954409712473922.

Muld, T., Efraimsson, G., Hennigson, D.S., 2013b. Mode decomposition and slip-stream velocities in the wake of two high-speed trains, Int. J. Railway Technol., accepted for publication.

Munson, B.R., Young, D.F., Okiishi, T.H., 2006. Fundamentals of Fluid Mechanics, fifth ed. John Wiley and Sons, Hoboken, New Jersey, USA.

Pauley, W.R., Eaton, J.K., 1988. Experimental study of the development of long-itudinal vortex pairs embedded in a turbulent boundary layer. AIAA J. 26 (7), 816–823.

Pii, L., Vanoli, E., Polidoro, F., Gautier, S., Tabbal, A., 2014. A full scale simulation of a high speed train for slipstream prediction. In: Proceedings of the Transport Reserach Arena, Paris, France.

Pope, C.W., 2007. Effective Management of Risk from Slipstream Effects at Trackside and Platforms. Rail Safety and Standards Board – T425 Report.

Roshko, A., 1955. On the wake and drag of bluff bodies. J. Aeronaut. Sci. 22, 124–132.

Schober, M., Weise, M., Orellano, A., Deeg, P., Wetzel, W., 2010. Wind tunnel investigation of an ice3 endcar on three standard ground scenarios. J. Wind Eng. Ind. Aerodyn. 98, 345–352.

Schulte-Werning, B., Heine, B., Matschke, C., 2001. Slipstream development and wake flow characteristics of modern high-speed trains. J. Appl. Math. Mech. 81 (S3), 789–790.

Schulte-Werning, B., Heine, B., Matschke, C., 2003. Unsteady wake flow character-istics of high-speed trains. Proc. Appl. Math. Mech. 2, 332–333.

Sterling, M., Baker, C.J., Jordan, S.C., Johnson, T., 2008. A study of the slipstreams of high-speed passenger trains and freight trains. Proc. Inst. Mech. Eng. Part F: J. Rail Rapid Transp. 222, 177–193.

Strachan, R.K., Knowles, K., Lawson, N.J., 1988. The Effect of a Moving Floor on Wind-Tunnel Simulation of Road Vehicles. SAE Technical Paper No. 880245.

Weise, M., Schober, M., Orellano, A., 2006. Slipstream velocities induced by trains. In: Proceedings of the WSEAS International Conference on Fluid Mechanics and Aerodynamics, Elounda, Greece.

Westphal, R.V., Mehta, R.D., 1989. Interaction of an oscillating vortex with a turbulent boundary layer. Exp. Fluids 7, 405–411.

Yao, S., Sun, Z., Guo, D., Chen, D., Yang, G., 2013. Numerical study on wake characteristics of high-speed trains. Acta Mech. Sin. 29 (6), 811–822.